



JWST MIRI MRS Observations of T Cha: Discovery of a Spatially Resolved Disk Wind

Naman S. Bajaj¹ , Ilaria Pascucci¹ , Uma Gorti^{2,3} , Richard Alexander⁴ , Andrew Sellek^{5,6} , Jane Morrison⁷,
Andras Gaspar⁷ , Cathie Clarke⁵ , Chengyan Xie¹ , Giulia Ballabio^{8,9} , and Dingshan Deng¹

¹Lunar and Planetary Laboratory, The University of Arizona, Tucson, AZ 85721, USA; namanbajaj@arizona.edu

²NASA Ames Research Center, Moffett Field, CA 94035, USA

³Carl Sagan Center, SETI Institute, Mountain View, CA 94043, USA

⁴School of Physics and Astronomy, University of Leicester, University Road, Leicester LE1 7RH, UK

⁵Institute of Astronomy, Madingley Road, Cambridge CB3 0HA, UK

⁶Leiden Observatory, Leiden University, 2300 RA Leiden, The Netherlands

⁷Steward Observatory, The University of Arizona, Tucson, AZ 85721, USA

⁸Astronomy Unit, School of Physics and Astronomy, Queen Mary University of London, London E1 4NS, UK

⁹Astrophysics Group, Imperial College London, Blackett Laboratory, Prince Consort Road, London SW7 2AZ, UK

Received 2023 December 22; revised 2024 January 22; accepted 2024 January 23; published 2024 March 4

Abstract

Understanding when and how circumstellar disks disperse is crucial to constrain planet formation and migration. Thermal winds powered by high-energy stellar photons have long been theorized to drive disk dispersal. However, evidence for these winds is currently based only on small ($\sim 3\text{--}6\text{ km s}^{-1}$) blueshifts in [Ne II] 12.81 μm lines, which does not exclude MHD winds. We report JWST MIRI MRS spectro-imaging of T Cha, a disk with a large dust gap (~ 30 au in radius) and blueshifted [Ne II] emission. We detect four forbidden noble gas lines, [Ar II], [Ar III], [Ne II], and [Ne III], of which [Ar III] is the first detection in any protoplanetary disk. We use line flux ratios to constrain the energy of the ionizing photons and find that argon is ionized by extreme ultraviolet, whereas neon is most likely ionized by X-rays. After performing continuum and point-spread function subtraction on the integral field unit cube, we discover a spatial extension in the [Ne II] emission off the disk continuum emission. This is the first spatially resolved [Ne II] disk wind emission. The mostly ionic spectrum of T Cha, in combination with the extended [Ne II] emission, points to an evolved stage for any inner MHD wind and is consistent with the existence of an outer thermal wind ionized and driven by high-energy stellar photons. This work acts as a pathfinder for future observations aiming at investigating disk dispersal using JWST.

Unified Astronomy Thesaurus concepts: Planet formation (1241); Protoplanetary disks (1300); T Tauri stars (1681); Infrared spectroscopy (2285)

Supporting material: data behind figure

1. Introduction

According to the classic picture of protoplanetary disk evolution, disk material is depleted through viscous accretion onto the star (e.g., Hartmann et al. 2016) and via thermal winds (also known as photoevaporative, PE, winds; e.g., Alexander et al. 2014). Viscous accretion is a process in which the gas viscosity (or turbulent stresses) creates friction between different layers of material, causing a shearing motion. The energy of the shearing motion is dissipated as heat, and the gas falls deeper in the potential well, causing it to accrete onto the star (e.g., Pringle 1981; Ruden & Pollack 1991). On the other hand, PE winds are gaseous outflows driven away from the disk due to high-energy ($>6\text{ eV}$) radiation from the star. These winds are only expected to originate outward of $\sim 0.1\text{--}0.2 r_G$, where r_G is the gravitational radius where the thermal energy becomes large enough to overcome the gravitational potential of the star (e.g., Gorti et al. 2016). When the accretion rate falls below the PE wind mass-loss rate, the gas supply to the inner disk is limited, and a gap is opened, after which the disk is quickly cleared from the inside out (e.g., Clarke et al. 2001). In this scenario, there is an intermediate short-lived stage of a protoplanetary disk where there is a large gap in the gas and

dust (see, e.g., Ercolano & Pascucci 2017, for a discussion). It has also been shown through several studies that the interaction of planets with the disk can excite a spiral structure, which can then generate shocks and open a gap (see Bae et al. 2023, for a recent review). However, regardless of whether these gaps are formed by photoevaporation or planets, constraining the PE wind mass-loss rate will inform us of the lifetime of the gas disk, which in turn governs the time left for giant planet formation and migration (e.g., Testi et al. 2014).

More recently, disk simulations with detailed microphysics found that accretion is mainly driven by magnetohydrodynamic (MHD) disk winds (see, e.g., Lesur 2021; Lesur et al. 2023; Pascucci et al. 2023, for recent reviews). These MHD winds are magnetically induced gas flows that remove significant mass and angular momentum from the disk, leading to accretion onto the star. Along with theoretical advances, several disk wind diagnostics have been identified (see, e.g., Pascucci et al. 2023, for a review). Among them, we highlight here the [S II] 4068 \AA , [O I] 6300 \AA , and [Ne II] 12.81 μm lines. The wind-tracing nature of these lines is inferred by blueshifts (up to $\sim 20\text{ km s}^{-1}$) in their high-resolution spectra. Among these wind diagnostics, the [O I] $\lambda 6300$ line is studied in great detail as it is ubiquitously found in disk environments (e.g., Simon et al. 2016; Banzatti et al. 2018; Nisini et al. 2018; Fang et al. 2023a). For instance, in a survey of forbidden lines in 108 T Tauri stars in NGC 2264, McGinnis et al. (2018) found that 107 of them had an [O I] low-velocity Gaussian component



Original content from this work may be used under the terms of the [Creative Commons Attribution 4.0 licence](https://creativecommons.org/licenses/by/4.0/). Any further distribution of this work must maintain attribution to the author(s) and the title of the work, journal citation and DOI.

($\sim 30 \text{ km s}^{-1}$) consistent with a disk wind. In another survey using high-resolution spectroscopy, Pascucci et al. (2020) modeled the [O I] $\lambda 6300$ low velocity from several transition disks and showed that most of the emission is coming from within $\sim 1\text{--}2 \text{ au}$. More recently, Fang et al. (2023b) spatially resolved the [O I] $\lambda 6300$ emission from TW Hya and showed that 80% comes from within 1 au of the star, in agreement with previous inferences based on modeling spectrally resolved [O I] profiles (Pascucci et al. 2011, 2020). The small emitting radius in TW Hya as well as in other sources, combined with blueshifts in the line centroids, are difficult to reconcile with the PE wind scenario (but see Rab et al. 2023), and [O I] is therefore more frequently interpreted as tracing an MHD disk wind (e.g., Simon et al. 2016; Banzatti et al. 2019; Fang et al. 2023a).

On the other hand, the [Ne II] $12.81 \mu\text{m}$ detections using Spitzer (Espaillat et al. 2007; Lahuis et al. 2007; Pascucci et al. 2007) at the time of discovery were spectrally unresolved. However, follow-up ground-based high spectral resolution observations of [Ne II] $12.81 \mu\text{m}$ demonstrated that it is an important diagnostic of disk winds (e.g., Herczeg et al. 2007; Pascucci & Sterzik 2009; Baldovin-Saavedra et al. 2012; Sacco et al. 2012). Disks with inner dust cavities show singly peaked [Ne II] profiles with modest widths (FWHM $\sim 15\text{--}40 \text{ km s}^{-1}$) and small blueshifts ($\sim 3\text{--}6 \text{ km s}^{-1}$) relative to the stellar systemic velocity (Pascucci & Sterzik 2009; Sacco et al. 2012) that are consistent with the PE wind model predictions (Alexander 2008). Additionally, the absence of the redshifted component of [Ne II] suggests that there is dust in the midplane, which blocks our view of the receding wind (Alexander 2008; Ercolano & Owen 2010; Pascucci et al. 2011), and that the emission originates largely outside the dust hole.

However, line profiles alone cannot determine whether [Ne II] also traces MHD disk winds. Furthermore, they cannot discriminate between PE winds driven by extreme-ultraviolet (EUV; Alexander 2008) and X-ray radiation (Ercolano & Owen 2010), i.e., wind mass-loss rates that differ by 2 orders of magnitude. Unlike [O I], the [Ne II] emission has never been spatially resolved to analyze whether it is tracing emission from the very inner regions of the disk ($< 1\text{--}2 \text{ au}$, similar to [O I]) or if it is tracing a more extended emission. This is important because PE winds cannot be driven from the very inner regions ($< 1\text{--}2 \text{ au}$ for solar-mass stars), which are too deep into the gravitational potential well of the star for the gas to escape (e.g., Hollenbach et al. 1994; Font et al. 2004; Clarke & Alexander 2016). On the contrary, MHD winds can easily be driven from these very inner regions close to the star and can also extend outward up to tens of au (e.g., Gressel et al. 2015; Béthune et al. 2017). Hence, by observing the radial extent of [Ne II] emission in a disk with a very small inner disk and a large dust gap, it can be shown whether the wind is compact or extended. From such a disk, an unresolved, i.e., compact emission would suggest that [Ne II] is tracing an MHD wind. On the other hand, a resolved extended emission would be compatible with both the PE wind scenario and radially extended MHD wind models.

To test this hypothesis, we employ MIRI Medium Resolution Spectroscopy (MRS) to observe T Cha, a young T Tauri star surrounded by a disk with a large dust cavity, and test whether the known [Ne II] emission is spatially extended. The paper is organized as follows. In Section 2, we provide details of the source, observations, and calibration technique employed

to reduce the data. In Section 3, we detail the analysis and present our results demonstrating that [Ne II] emission is spatially extended in T Cha (Section 3.2). We discuss our results in Section 4 and summarize this work in Section 5.

2. Source, Observations, and Calibration

2.1. Details about the Source

This study focuses on T Cha, a bright G8 spectral type star (Chavarría et al. 1989; Alcalá et al. 1993; Schisano et al. 2009) located at a distance of $\sim 103 \text{ pc}$ as calculated using the Gaia Data Release 3 (Gaia Collaboration et al. 2023) and a member of the ϵ Cha association (see Murphy et al. 2013; Dickson-Vandervelde et al. 2021, for a recent examination of the ϵ Cha membership). The estimated age of T Cha has a large range and is estimated to be between 2 and 10 Myr (Fernández et al. 2008; Ortega et al. 2009), similar to the age range reported for ϵ Cha ($\sim 3\text{--}8 \text{ Myr}$; Dickson-Vandervelde et al. 2021). The primary reason for selecting T Cha as a target for our MIRI MRS observation is its strong [Ne II] $12.81 \mu\text{m}$ detection (Lahuis et al. 2007) with a small blueshift in the centroid velocity ($\sim 3\text{--}6 \text{ km s}^{-1}$) and a line width of $\sim 40 \text{ km s}^{-1}$ indicating that it is tracing a disk wind (Pascucci & Sterzik 2009; Sacco et al. 2012). Pascucci & Sterzik (2009) could fit this [Ne II] line profile very well with the PE wind model from Alexander (2008), assuming that T Cha is a nearly edge-on disk and the gas disk does not have a gap. Later, both assumptions were found to be true: the disk of T Cha is viewed at an inclination angle of $\sim 70^\circ$ (Huélamo et al. 2015; Pohl et al. 2017; Hendlér et al. 2018), and no gap is detected in the gas disk (Huélamo et al. 2015; Wölfer et al. 2023). The absence of a gap is consistent with the fact that the star is accreting, with an accretion rate of $\sim 4 \times 10^{-9} M_\odot \text{ yr}^{-1}$ (Cahill et al. 2019). In contrast to the gas component, the dust disk has a large gap from ~ 1 to 20 au and an outer ring from ~ 20 to 50 au (Olofsson et al. 2013; Pohl et al. 2017; Hendlér et al. 2018).

In addition to the high-resolution ($R \sim 600$) Spitzer InfraRed Spectrograph (IRS) spectrum that revealed a strong [Ne II] line at $12.81 \mu\text{m}$ (Lahuis et al. 2007), T Cha was also observed in the low-resolution ($R \sim 105$) mode (Kessler-Silacci et al. 2006). The polycyclic aromatic hydrocarbon (PAH) feature at $11.2 \mu\text{m}$ is clearly detected in the low-resolution mode (Geers et al. 2006; Kessler-Silacci et al. 2006), while the [Ne III] line at $15.55 \mu\text{m}$ is barely detected in the high-resolution mode (Lahuis et al. 2007). The [Ar II] and [Ar III] lines at 6.98 and $8.99 \mu\text{m}$ are not detected at low resolution, although [Ar II] was predicted to be as strong as [Ne II] (Hollenbach & Gorti 2009).

2.2. Observations and Data Calibration Details

T Cha was observed as part of the Cycle 1 General Observer program (proposal ID: 2260; PI: I. Pascucci) using the MIRI MRS instrument on board the James Webb Space Telescope (JWST; Wells et al. 2015). It was observed on 2022 August 13–14 for 3.24 hr on-source and 4.48 hr including the over-heads. We used a four-point dither pattern optimized for an extended source around the central position of T Cha: R.A. (J2000) 11:57:13.5269 and decl. (J2000) $-79:21:31.52$. The source acquisition was not employed, as the aim was to perform spectral mapping of an extended source. The integral field unit (IFU) data were taken in all three bands (SHORT, MEDIUM, and LONG) in all four channels covering the entire MRS wavelength range of $\sim 4.9\text{--}28 \mu\text{m}$.

There were 14 integrations per dither point, which sums to a total of 56 integrations for four dither pointings. A total of 25 groups were taken in FASTR1 mode per integration, and the integration time per MRS subband and complete dither was 4030 s. A dedicated background was also observed using identical settings as for T Cha. A nearby field was chosen as a background owing to the fields' relative deficiency of astronomical sources using the Wide-field Infrared Survey Explorer all-sky catalog (Wright et al. 2010).

We used version 1.11.2 of the JWST calibration pipeline (Bushouse et al. 2023), which was the latest version made available as of 2023 July 12. This version uses the updated MRS spectral response function part of the Spec2Pipeline and the improved cube building and outlier detection step of the Spec3Pipeline. We used the Calibration Reference Data System (CRDS) version 11.16.21 and context "jwst_1100.pmap" for reference files and their selection rules, respectively.

The fringe correction step is executed using a fringe flat field and is included in the pipeline as part of the Spec2Pipeline. We further reduced the fringing by applying the residual_fringe step (P. Kavanagh et al. 2024, in preparation), which is included in the JWST calibration pipeline package as part of Spec2Pipeline but switched off by default. We used the outlier_detection step of the Spec3Pipeline, which successfully removes bad pixels from the data. We compared three different methods of background subtraction: (a) pixel-by-pixel subtraction before cube creation as part of the Spec2Pipeline, (b) uniform model background subtraction as part of the Spec3Pipeline, and (c) pixel-by-pixel subtraction after cube creation postpipeline. Among these, method (c) reduced fringing at longer wavelengths as well as the number of outliers, and hence we adopted method (c) for our background subtraction. Looking at the IFU cubes, we find that T Cha is not centered in the field of view. This is because the effect of the proper motion from the J2000 coordinates was not accounted for during the observation. However, we safely retain all the source emission in all four channels owing to which we obtain a spectrum for T Cha for the complete wavelength range of MIRI MRS ($\sim 5\text{--}28\ \mu\text{m}$). After creating a pixel-by-pixel background-subtracted IFU cube, we retrieve a 1D spectrum by summing all the pixels in an aperture of radius $2.5 \times \text{FWHM}$, where $\text{FWHM} = 0.033 \times (\lambda/\mu\text{m}) + 0''.106$ (Law et al. 2023). We perform the aperture correction after extracting the spectrum, with values retrieved from the aperture correction reference file in CRDS.

One of the key science goals of our program was to evaluate if emission in lines known to trace disk winds is extended. As such, in addition to inspecting 1D spectra, we perform spaxel-by-spaxel continuum subtraction (Section 3.2.1) as well as point-spread function (PSF) subtraction (Section 3.2.2) in selected emission lines. We use the standard star HD 37962, which is a bright G2V star, as a proxy for the PSF. HD 37962 was observed under proposal ID 1538, also noted as CAL-FLUX-003, which is an absolute flux calibration program (Gordon et al. 2022). HD 37962 was observed with a four-point dither, similar to T Cha, for ~ 2.2 hr including the overheads. A dedicated background was also observed for HD 37962 for ~ 0.7 hr using a two-point dither. Both observations covered the whole wavelength range of MIRI MRS ($\sim 5\text{--}28\ \mu\text{m}$) and used the FAST readout mode. We obtained

the uncalibrated raw files for both observations using the Barbara A. Mikulski Archive for Space Telescopes (MAST¹⁰) and calibrated them using the same methodology as for T Cha, except for the background-subtraction step. As HD 37962 and its background are observed in different dither configurations, we could not perform pixel-by-pixel subtraction and instead performed the master background subtraction, which is available as part of the Spec3_pipeline.

To take into account the MIRI MRS PSF variations and their impact on our results, we perform the PSF comparison and subtraction with an additional standard star, HD 167060, which is a G3V star and was observed the same day as T Cha: 2022 August 14. HD 167060 was observed under the same program (1538) as HD 37962 for ~ 2.8 hr with a dedicated background observed for ~ 0.6 hr including the overheads. The observation settings and data reduction techniques employed for HD 167060 are the same as for HD 37962.

3. Analysis and Main Results

Here we discuss the detection of four forbidden noble gas lines with the first-ever detection of [Ar III] in a protoplanetary disk. We also describe the two independent methods employed for discovering the spatially extended emission in [Ne II].

3.1. Detection of Multiple Transitions from Ionized Noble Gases

In accordance with previous observations, we have a strong detection of the [Ne II] $12.81\ \mu\text{m}$ line in the JWST MIRI MRS spectrum of T Cha. We also detect the [Ne III] 15.55 , [Ar II] 6.98 , and [Ar III] $8.99\ \mu\text{m}$ emission lines as shown in Figure 1, making it the first-ever spectrum of a protoplanetary disk to have detected four forbidden noble gas lines together. Additionally, we also detect PAH bands at 6.02 and $8.22\ \mu\text{m}$ as well as PAH complexes at 6.2 , 7.7 , 8.6 , 11.3 , 12 , and $12.7\ \mu\text{m}$, of which only the $11.2\ \mu\text{m}$ complex was detected for T Cha using Spitzer (Geers et al. 2006; Kessler-Silacci et al. 2006). Furthermore, we detect the $\text{H}_2\nu 0\text{--}0\ \text{S}(3)$ line at $9.66\ \mu\text{m}$ and do not detect the most commonly detected hydrogen recombination line H I (7-6) at $12.37\ \mu\text{m}$ (e.g., Rigliaco et al. 2015).

To calculate the line fluxes and their uncertainties, we adopt a Monte Carlo approach. First, we fit a straight line to ~ 20 data points outside the transition on either side and calculate the standard deviation relative to the fitted line. Then, a set of 10,000 spectra is generated within the range of a Gaussian distribution with a sigma for each point equal to the previously calculated standard deviation. For all of the spectra, we fit a Gaussian profile and compute the area under the curve. We use the mean and standard deviation of these areas as the final flux and the associated uncertainty, respectively (e.g., Pascucci et al. 2008; Banzatti et al. 2012). To calculate the upper limits in case of nondetections, we use the equation

$$F_{\text{up}} = 3\sigma d_{\lambda} \sqrt{N}, \quad (1)$$

where σ is the rms of the data points where the line would have been, and the line flux is computed over the spectral resolution element ($N = 2$ pixels), assuming the noise is uncorrelated.

¹⁰ MAST is a NASA-funded project to support and provide a variety of astronomical data archives, with the primary focus on the optical, ultraviolet, and near-infrared parts of the spectrum. MAST is located at the Space Telescope Science Institute (STScI).

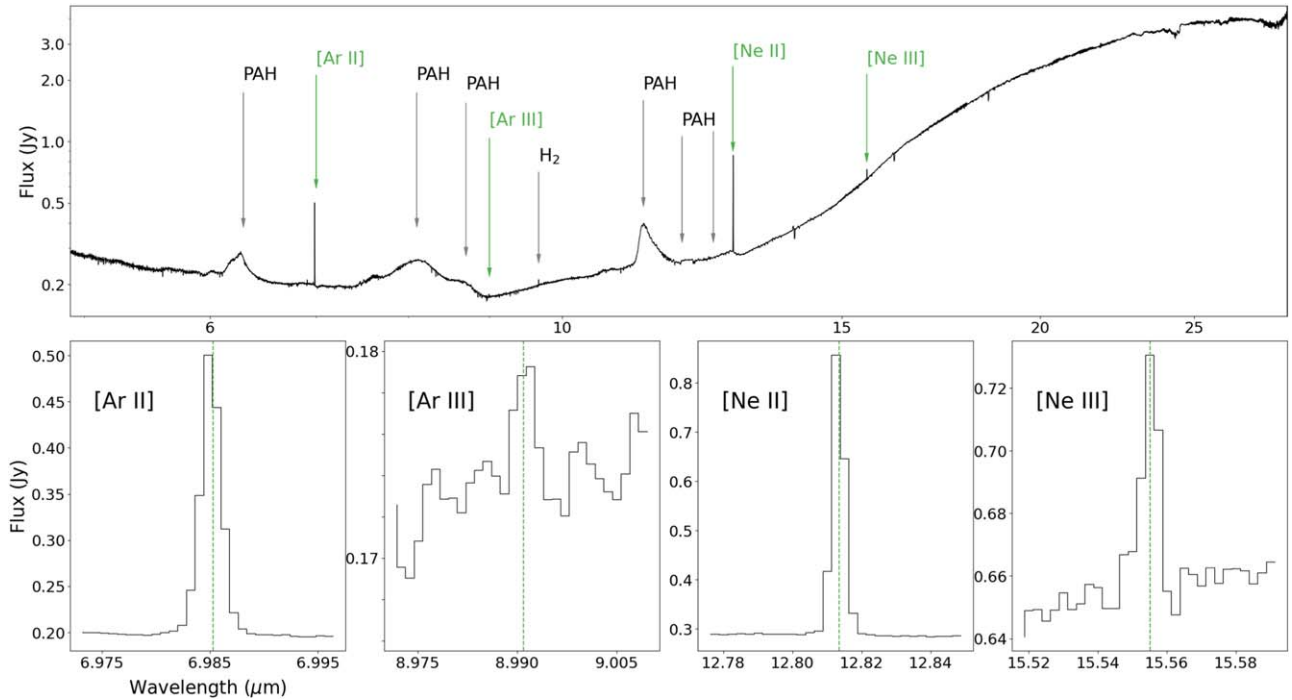


Figure 1. The upper panel is the JWST MIRI MRS spectrum of T Cha plotted between ~ 5 and $\sim 28 \mu\text{m}$ with the PAH features and $\text{H}_2 v=0-0 \text{S}(3)$ line marked in black and the forbidden noble gas emissions in green. The lower four panels further highlight the four forbidden line emissions, [Ar II], [Ar III], [Ne II], and [Ne III], which will be the focus of this study.

(The data used to create this figure are available.)

Table 1
Measured Line Fluxes, 3σ Upper Limits, and Continuum Level

Line	Wavelength ^a (μm)	This Work		Published Spitzer	Continuum Level ^c	
		JWST	Spitzer ^b ($10^{-14} \text{ erg s}^{-1} \text{ cm}^{-2}$)		JWST	Spitzer
[Ar II]	6.98	4.31 ± 0.02	<10.5	$<10.68^{\text{d}}$	0.2	0.69
[Ar III]	8.99	0.08 ± 0.02	<0.81	...	0.175	0.455
$\text{H}_2 \text{S}(3)$	9.66	0.13 ± 0.01	<0.8	...	0.195	0.41
H I (7-6)	12.37	<0.15	<0.9	...	0.27	0.32
[Ne II]	12.81	4.99 ± 0.01	3.2 ± 0.2	$3.2 \pm 0.2^{\text{e}}$	0.29	0.3
[Ne III]	15.55	0.52 ± 0.02	<0.5	$<0.2^{\text{e}}$	0.655	0.3
PAH ^f	6.2	95.4	0.23	0.82
PAH ^f	11.2	104	41	33^{g}	0.26	0.38

Notes. The reported 1σ uncertainty for the JWST spectra should be added in quadrature with the absolute flux error ($\sim 5\%$; Argyriou et al. 2023).

^a Rest wavelength of the line.

^b Recalculated values in this work using the Spitzer IRS high-res spectrum ($R \sim 700$).

^c Continuum flux at the rest wavelength of the corresponding lines.

^d Published value from Szulágyi et al. (2012).

^e Published values from Lahuis et al. (2007).

^f The flux is calculated as the area under the feature without fitting a Gaussian profile.

^g Published value from Geers et al. (2006).

Here, d_λ is the wavelength of the given line divided by the resolution (see Szulágyi et al. 2012, for a similar approach). These integrated fluxes and upper limits from the MIRI spectrum of T Cha are listed in Table 1 along with the estimates from the Spitzer IRS spectrum, calculated using the same technique. We do not detect H I (7-6) and provide an upper limit in Table 1. The nondetection of the H I (7-6) line aligns

with the low H I (7-6)/[Ne II] ratio of 0.008 expected for disk winds (see Hollenbach & Gorti 2009). Even in the scenario where H I (7-6) traces accretion (see Rigliaco et al. 2015), T Cha has a weaker emission than average given its accretion luminosity. This may be due to the H I emission being partly obscured by the nearly edge-on disk of T Cha, which was also suggested to explain low $\text{H}\alpha$ emission by Cahill et al. (2019).

A Gaussian fit to each of the lines listed, including H I (7-6), is described in Appendix A.

Using the method described above, we report a 4σ detection of [Ar III], accompanied by a $>10\sigma$ detection of both [Ne III] and H₂ S(3). The most robust detections, [Ar II] and [Ne II], exhibit signals exceeding 200σ . Owing to the strong detections of [Ar II] and [Ne II], we focus on exploring any spatial extension in these lines.

3.2. Spatially Extended [Ne II] Wind Emission

As mentioned in Section 2, high-resolution ground-based spectroscopy demonstrated that the [Ne II] at $12.81\ \mu\text{m}$ from T Cha is slightly blueshifted ($\sim 4\ \text{km s}^{-1}$) relative to the stellar velocity and hence likely tracing a slow disk wind (Pascucci & Sterzik 2009; Sacco et al. 2012). Here, we further show that the [Ne II] emission is spatially extended by employing two different techniques to isolate the line emission and compare it with the PSF.

3.2.1. Spaxel-by-spaxel Continuum Subtraction

In this first approach, we remove the continuum in each spaxel to generate line-only maps. To do this, we consider ~ 30 continuum data points on both sides of the line emission and curve-fit an n -degree polynomial, such that n is the lowest integer that best fits the data. In the case of T Cha, we can use a second-order polynomial. For wavelength points in a spaxel under consideration, we subtract a two-order polynomial continuum model flux and create a corresponding continuum-subtracted cube. Simultaneously, using the polynomial continuum model flux for each wavelength point in a spaxel, we create a continuum emission cube too (see Beck & Bary 2019, for a similar method applied to H₂ rovibrational lines). We repeat this procedure and regenerate the continuum and continuum-subtracted data cubes for each line individually. Each time, our continuum fit is good only for the ~ 30 points considered on both sides of the line and likely poor anywhere beyond it. We apply this procedure to all three strongly detected forbidden lines (except [Ar III], owing to its relatively weak detection of $\sim 4\sigma$) to create their continuum-subtracted maps.

For each of these continuum-subtracted line maps, we select the wavelength plane with the peak line emission and fit a 2D Gaussian to determine the size and position angle (PA) of the emission. We also fit a 2D Gaussian to the corresponding wavelength plane in each of the continuum maps. We perform this 2D Gaussian fitting using the `imfit` task, which is part of the Common Astronomy Software Application (CASA; McMullin et al. 2007) package. We apply the same approach to the standard star (HD 37962) at the peak line wavelengths of the [Ar II], [Ne II], and [Ne III] lines in T Cha to compare the component size for possible extension beyond a point source. HD 37962 was favored over HD 167060 owing to its comparatively higher luminosity. Results from our analysis are shown in Figure 2. Of the three wavelengths shown, the size of the standard star emission (PSF) is smallest at $7\ \mu\text{m}$ and largest at $15.55\ \mu\text{m}$, as expected since the PSF size increases linearly as a function of wavelength; see the relation in Section 2. At $7\ \mu\text{m}$, the size and PA of the standard star and the continuum-subtracted [Ar II] are similar within the error bars, suggesting compact [Ar II] emission. Similarly, the major axis of the nearby continuum and the PA are the same within the

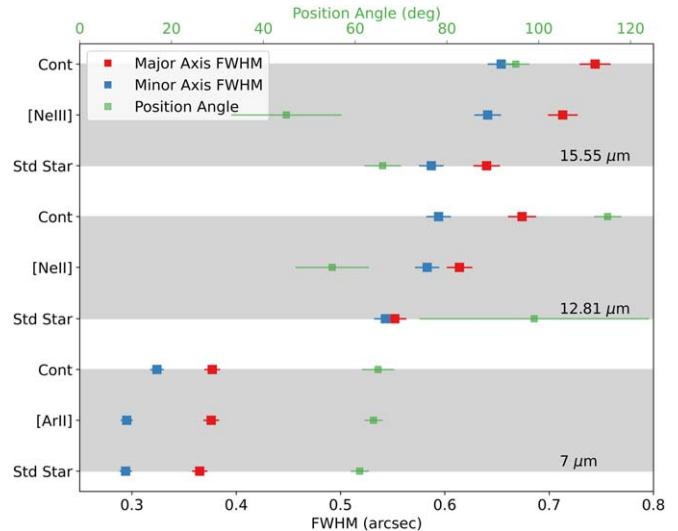


Figure 2. Comparison of the 2D Gaussian size calculated from images of the continuum-subtracted line, T Cha continuum (represented as Cont), and standard star (represented as Std Star). The three are compared at the same wavelength for [Ar II], [Ne II], and [Ne III], respectively.

error bars, suggesting a compact emission too; however, the minor axis is slightly larger than the PSF, hinting at a slightly resolved $7\ \mu\text{m}$ emission.

At $12.81\ \mu\text{m}$, the standard star is more circular and therefore has a large error bar associated with its PA. It is clear that the [Ne II] emission is more extended/resolved than the standard star, and the continuum is further extended than the [Ne II] emission. Note that the continuum PA at $12.81\ \mu\text{m}$ is $115^\circ \pm 3^\circ$, which is in strong agreement with the previous estimates of the disk PA: $113^\circ \pm 6^\circ$ (Huélamo et al. 2015; using the Atacama Large Millimeter/submillimeter Array, ALMA, CO (3-2) integrated emission map), $\sim 113^\circ$ (Hendler et al. 2018; using the ALMA dust continuum at 3 mm), and $\sim 114^\circ$ (Pohl et al. 2017; using Very Large Telescope, VLT, SPHERE observations of the dust disk). Importantly, not only is the [Ne II] emission more extended than the standard star, it also fits a significantly different PA than the T Cha continuum, signaling that [Ne II] is tracing emission away from the disk. This further corroborates the disk wind hypothesis inferred from the spectrally resolved [Ne II] profiles. At $15.55\ \mu\text{m}$, we see similar results as for [Ne II]. Specifically, the [Ne III] emission is significantly extended beyond the standard star, and its PA is the same within the error bars as the [Ne II] and different from the continuum. The continuum too at $15.55\ \mu\text{m}$ is extended beyond the standard star, as would be expected considering the extension in the $12.81\ \mu\text{m}$ continuum. We note that the disk PA inferred from the $15.55\ \mu\text{m}$ continuum emission does not agree with that at $12.81\ \mu\text{m}$. We speculate that this may be due to the degradation in spatial resolution at longer wavelengths, such that the extension in the continuum emission is less reliable at 15.55 than at $12.81\ \mu\text{m}$.

It is also interesting to note that when this same method is applied to the PAH features, particularly the one centered around $6.2\ \mu\text{m}$, we find that these features, too, are more extended compared to the standard star. We find that these PAH features are more extended than the continuum at that wavelength, too—the Gaussian size of the $6.2\ \mu\text{m}$ PAH emission is $0''.4 \times 0''.36$, while that of the standard star and continuum is $0''.35 \times 0''.28$.

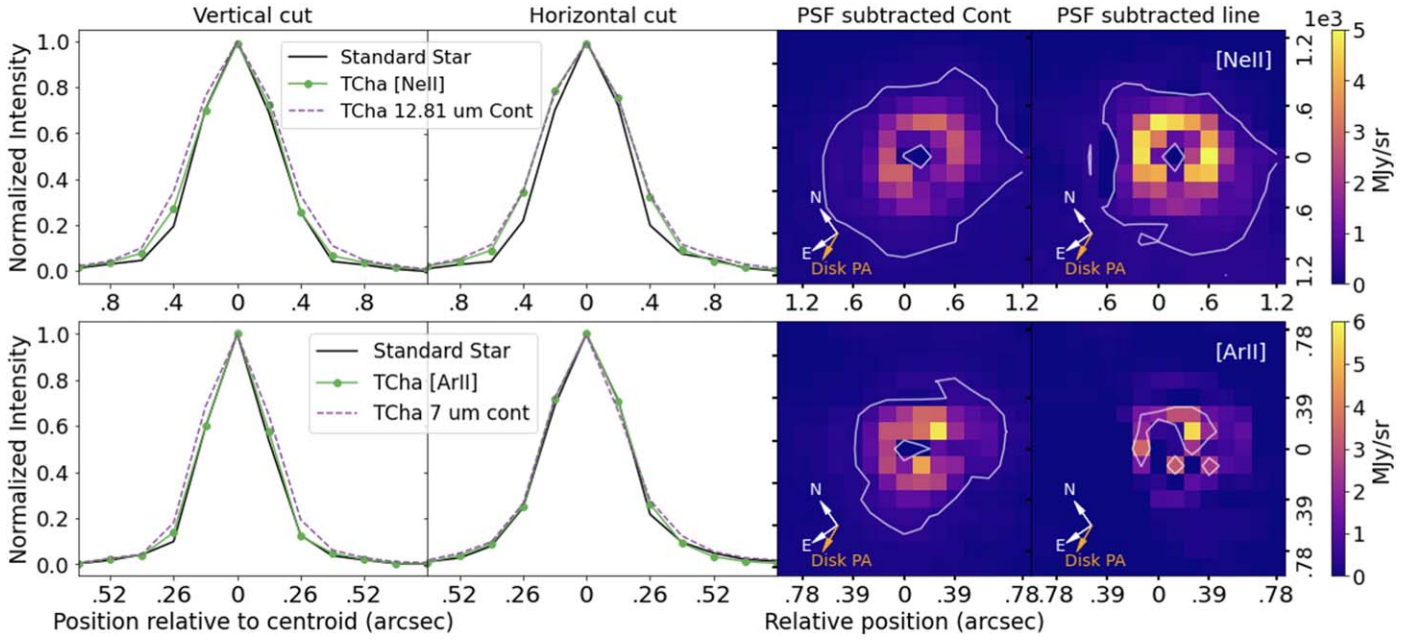


Figure 3. The left two panels compare the radial profiles of continuum and continuum-subtracted lines with the PSF (standard star HD 37962) in the horizontal and vertical directions. The two panels on the right show the PSF-subtracted images of the continuum at 12.81 and 7 μm and the [Ne II] and [Ar II] lines. The white contours in the PSF-subtracted images follow $5\times$ the rms calculated in the source-emission-free regions in the PSF-subtracted images.

3.2.2. PSF Subtraction

We perform PSF comparison as well as subtraction to test the results reported in the previous subsection independently. When we conduct PSF subtraction on the [Ne II] line emission, we find it to be spatially resolved in agreement with the results from Gaussian fitting. We treat the same standard star observation used in the previous section, HD 37962, as the PSF. To effectively compare our observations with the PSF, we reduce the observations in the detector plane using the “ifualign” mode during cube building. Though T Cha is off-center in the detector plane, it does not affect our routine, as no field-dependent distortion has been seen for the PSF of MIRI MRS (P. Patapis 2023, personal communication) so far. To perform PSF comparison, we first find the image centroid for the line image as well as the PSF using the `centroid_2dg` function part of Photutils.¹¹ Using the centroid, both sources are shifted such that the centroid lies at the center of their respective images. This step is carried out using the `interpolation.shift` utility of the `scipy.ndimage` package, which is very well tested in a broad range of applications. The interpolation function used is bicubic spline. Next, we scale the PSF emission to the line emission by using a weighted average ratio of a 5×5 pixel grid around the central spaxel.

We compare the scaled PSF with the continuum and line emission at 12.81 and 7 μm by drawing radial profiles in horizontal and vertical directions passing through the central bright pixel (see the left half of Figure 3). We try to perform the same analysis on [Ne III] as well; however, the emission in the continuum-subtracted image is not strong enough to find its centroid with confidence. Hence, we restrict our analysis to [Ne II] and [Ar II]. At 12.81 μm , both the vertical and horizontal profiles of the continuum as well as [Ne II] show extension beyond the PSF profile. However, at 7 μm , only the

continuum is slightly extended beyond the PSF in the vertical profile. The [Ar II] emission in both the vertical and horizontal profiles closely follows the PSF. It should be noted that, in both cases, the continuum is more extended than the line emission in the vertical direction, as expected since the disk orientation is close to being vertical in the image plane considering its PA of $\sim 115^\circ$ from north shown in Figure 3.

To corroborate these results using the 2D image, we subtract the scaled PSF image from the continuum and line images, respectively. These PSF-subtracted images at 12.81 and 7 μm are shown in Figure 3 (right half). The white contours trace $5\times$ the rms calculated in a PSF-sized aperture away from the source in the PSF-subtracted images. The contours clearly show that [Ne II] traces extended emission beyond the PSF. As can be seen, the continuum at 12.81 μm is also well resolved and shows a broad emission. It is important to note that, when looked at closely, the direction of extension in [Ne II] is not the same as the direction of extension in the continuum image, suggesting that [Ne II] is tracing an emission away from the disk, which is compatible with a wind. This is much more clearly seen in the difference of their PA in Figure 2, as also mentioned earlier. To estimate the component size of [Ne II] emission, we subtract the PSF FWHM in quadrature with [Ne II] FWHM in both horizontal (wind) and vertical (\sim disk) directions. This results in $0''.32$ in the wind direction and $0''.13$ in the disk direction, which translates to ~ 33 and ~ 13 au at a distance of 103 pc. At 7 μm , however, the continuum is only slightly resolved, and [Ar II] very clearly traces a much more compact emission, as was also seen through the vertical and horizontal curves investigated earlier and through the 2D Gaussian fit to the continuum-subtracted image in Figure 2.

We also demonstrate that our results are independent of the PSF variations by following the exact same procedure with the standard star HD 167060. An analysis similar to Figure 3 is shown in Figure 7 in the Appendix but for HD 167060. It is clear that at 12.81 μm , both the continuum and [Ne II] are

¹¹ Photutils is an Astropy package for detection and photometry of astronomical sources (Bradley et al. 2022).

extended in different directions, and at $7\ \mu\text{m}$, [Ar II] shows compact emission, consistent with the results described above. See Appendix B for details on PSF subtraction with HD 167060 as the standard star.

Additionally, we perform this method on the $6.2\ \mu\text{m}$ PAH feature and find it to be spatially extended, in agreement with the result from the continuum subtraction presented in the previous subsection. We present this result for $6.2\ \mu\text{m}$ PAH in Appendix C.

4. Discussion

Through the MIRI MRS observation of T Cha, we found several forbidden noble gas lines, which possibly trace disk winds, and many PAH emission bands along with the $\text{H}_2\text{v}0\text{-}0\ \text{S}(3)$ line. Among these lines, [Ne II] has been known as a disk wind tracer for over a decade (e.g., Pascucci & Sterzik 2009). We found that the JWST flux of [Ne II] in T Cha is higher than that of Spitzer. Additionally, the infrared continuum of T Cha has also changed considerably, as is evident from Table 1, which prompts us to contextualize the two results in Section 4.1. We also use line ratios to determine the main ionization source of these lines in Section 4.2.

Our analysis in Section 3.2 revealed that the [Ne II] and [Ne III] emission is extended beyond the PSF, while [Ar II] is not. In Section 4.3, we discuss these results in the context of PE and MHD winds. Finally, in Section 4.4, we discuss the nature of the extended PAH emission we reported in Section 3.2

4.1. The Origin of Continuum and Line Variability

The JWST and Spitzer T Cha continuum values in Table 1 clearly demonstrate that the disk is variable at infrared wavelengths. While the continuum flux density at $\sim 7\ \mu\text{m}$ has decreased by a factor of ~ 3 from 2006 to 2022, that at $\sim 16\ \mu\text{m}$ has increased by a factor of ~ 2 (see C. Xie et al. 2024, in preparation, for more details on the continuum variability). This type of variability has been reported for other disks (e.g., Espaillat et al. 2011), but it is typically smaller than that observed for T Cha. This means that for T Cha, during the JWST observations, there is less dust attenuation, and more stellar radiation could penetrate the inner disk and reach the outer disk than during the Spitzer time.

Interestingly, the pivot wavelength¹² of the seesaw variability is around $12.8\ \mu\text{m}$. While the continuum near the [Ne II] line has not changed, the line flux has increased from the Spitzer time by $\sim 50\%$ (see Table 1). This cannot be attributed to differences in the apertures used for spectral extraction because they are both large enough to encompass the entire emission— $3''.6$ for IRS and $2''.5$ diameter circle for MIRI MRS. The change in the [Ne II] flux is not as large as that observed by Espaillat et al. (2023) in SZ Cha ($\sim 150\%$), which, combined with the [Ne III] variability, was reasoned as a switch from EUV ionization to X-ray ionization of neon. However, this does not seem to be the case for T Cha, as its [Ne II]/[Ne III] ratio was > 1 even during the Spitzer time (Table 1), indicating ionization by X-rays (Section 4.2). The increase in T Cha’s [Ne II] emission might result from several factors, e.g., increase in the wind mass-loss rate, more heating, or higher fractional ionization. The latter two options are in line with the reduction of the inner disk mass (C. Xie et al. 2024, in preparation) and

the [Ne II] emission tracing emission out to the outer disk. However, a caveat with more heating is that it will enhance the emission only if the wind is colder than the excitation temperature ($< 1200\ \text{K}$).

T Cha is also highly variable at optical wavelengths (up to 3 mag in the V band; Covino et al. 1992; Alcalá et al. 1993; Walter et al. 2018), and so is the [O I] $\lambda 6300$ line (e.g., Covino et al. 1996). Dedicated monitoring has identified two different timescales for the [O I] variability: a short-term variability ($\sim 1\text{--}2$ days; Schisano et al. 2009) and a relatively long-term variability (≤ 2 yr; Cahill et al. 2019). Schisano et al. (2009) detected the short-term variability using three independent observation runs between 1993 and 1995 with observations in each run separated by less than a day. They found the variability timescale comparable to the optical photometric variations and also a positive correlation with the visual extinction. This led them to propose an “occluding clump” with a period of a few days and a maximum visual extinction magnitude of ~ 3.6 as a possible explanation for the optical continuum and line variabilities. On the other hand, Cahill et al. (2019) reported that the average [O I] 6300 line flux dropped from $1 \pm 0.1 \times 10^{-13}\ \text{erg cm}^{-1}\ \text{s}^{-2}$ recorded in 2012 to $0.3 \pm 0.4 \times 10^{-13}\ \text{erg cm}^{-1}\ \text{s}^{-2}$ recorded in 2014, suggesting a relatively “long-term” variability. This “long-term” variability cannot be explained by the occluding clump hypothesized by Schisano et al. (2009).

It is possible that the [Ne II] variability is similar to [O I] “short-term” and/or [O I] “long-term” variability; however, a visual extinction of ~ 3.6 mag will be too small at $\sim 13\ \mu\text{m}$ to produce the [Ne II] variability, making it more likely to be similar to the [O I] “long-term” variability. But having only two data points, i.e., Spitzer in 2006 and JWST in 2022, makes it difficult to derive any conclusion at present. Moreover, the nonalignment between the observation years of [O I] (~ 1993 , 2012, and 2014) and [Ne II] (2006 and 2022) further complicates comparing the evolution of these two lines relative to the disk evolution models of T Cha. Simultaneous monitoring of the two lines will be necessary to understand whether the [Ne II] and [O I] variabilities are correlated or not, the time period of each, and hence the underlying mechanism(s) for the variabilities.

4.2. Constraints on the High-energy Photons Impinging at the Disk Surface

The Ne^+ and Ar^+ ions detected in disks can only be ionized by stellar EUV ($13.6\ \text{eV} < h\nu < 100\ \text{eV}$) and/or X-ray ($0.1\ \text{keV} < h\nu < 10\ \text{keV}$) photons owing to their high ionization potentials (21.56 eV for neon and 15.76 eV for argon). It is crucial to determine the main source (EUV or X-ray) of disk heating and ionization, as it will constrain the wind mass-loss rate, which in turn will set a limit on the gas disk lifetime. [Ne II]/[Ne III] and [Ar II]/[Ar III] line intensity ratios can help discriminate between cases in which soft/hard EUV or soft/hard X-ray stellar photons provide the dominant source of disk atmosphere ionization (Hollenbach & Gorti 2009; Szulágyi et al. 2012; Espaillat et al. 2013). A hard spectrum is one in which there are more photons at higher energies beyond a certain energy value. Following the literature (e.g., Hollenbach & Gorti 2009), we define a hard X-ray spectrum as that in which there is a substantial contribution from photons at and beyond 1 keV and a soft X-ray spectrum as that in which flux dominates at 200–300 eV and declines at

¹² The wavelength at which there is no variability.

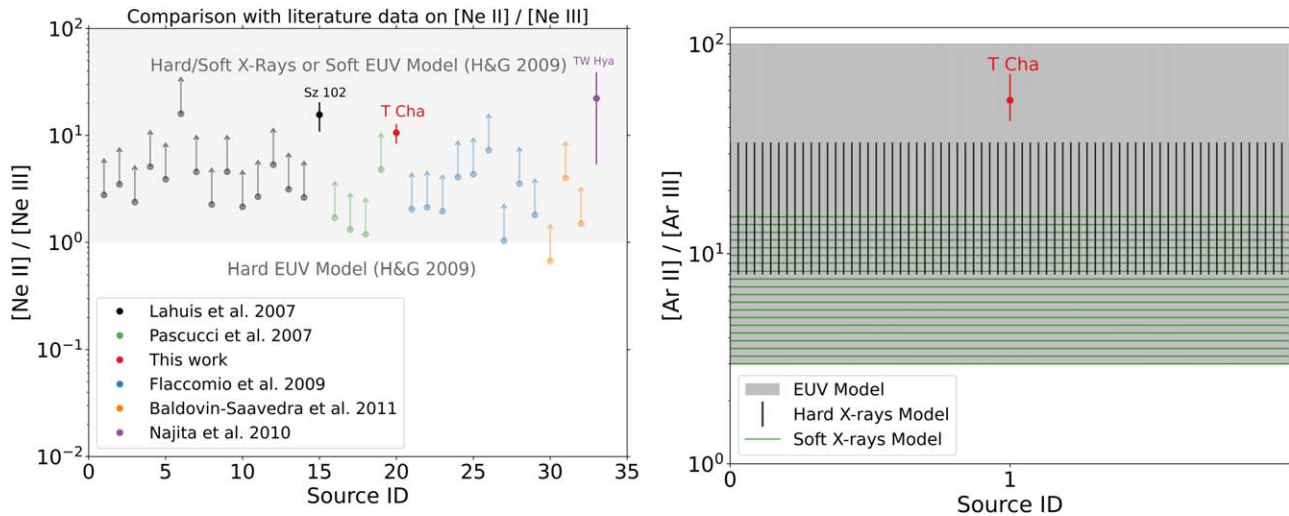


Figure 4. The left panel shows the $[\text{Ne II}]/[\text{Ne III}]$ ratio where the reference for each point is given in the legend, and the right panel shows the $[\text{Ar II}]/[\text{Ar III}]$ ratio for T Cha. Upward arrows indicate the lower limits, and H&G 2009 refers to Hollenbach & Gorti (2009). The white region in the left panel refers to the hard EUV model, which can easily be ruled out as the ionization source for neon. However, for argon, the right panel suggests that the EUV model is preferred over X-rays for its ionization. Here, the EUV model combines both soft and hard EUV radiation.

1 keV. For EUV, we consider a hard EUV spectrum as that in which $L(\nu) \propto \nu^{-1}$, whereas a soft EUV is a blackbody with $T \sim 20,000\text{--}30,000$ K.

We plot the $[\text{Ne II}]/[\text{Ne III}]$ and $[\text{Ar II}]/[\text{Ar III}]$ line ratios for T Cha in the context of previous Spitzer line detections and upper limits (see Figure 4). We overplot model predictions from Hollenbach & Gorti (2009) for $[\text{Ne II}]/[\text{Ne III}]$. For predicting the $[\text{Ar II}]/[\text{Ar III}]$ ratios, we used a TW Hya template stellar spectrum (Rauad & Gorti 2019) and models of Hollenbach & Gorti (2009). T Cha is the only object for which there are both ratios. While the $[\text{Ne II}]/[\text{Ne III}]$ plot only has three data points with both lines detected, the lower limits are sensitive enough to eliminate the possibility of hard EUV photons as the dominant neon ionization mechanism for all but one source. This is because the line luminosity ratio reflects the ion abundance ratios (see Hollenbach & Gorti 2009), given the nearly similar excitation energies and A values. Therefore, $[\text{Ne II}]/[\text{Ne III}] \sim f(\text{Ne}+)/f(\text{Ne}^{++})$, where f denotes the fraction of neon atoms in the respective ionization state. It is easier to produce $[\text{Ne III}]$ over $[\text{Ne II}]$ with hard EUV spectra, driving the ratio below 1, contrary to the observations. Soft EUV spectra (with $T < 30,000$ K) have few 41 eV photons to ionize $\text{Ne}+$ and therefore result in lower $[\text{Ne III}]$ emission. X-ray Auger ionization leads to multiply charged ions, which recombine rapidly and exchange charge with H atoms, leading to high $\text{Ne}+/\text{Ne}^{++}$ ratios (see Glassgold et al. 2007) for both hard and soft spectra as long as ~ 1 keV photons are present.

T Cha (this work) is the only source with both $[\text{Ar II}]$ and $[\text{Ar III}]$ detected. The line luminosity ratio is again approximately given by the ratio of the ion abundances to within a factor of $\lesssim 2$, and the observed line ratio therefore suggests that singly ionized argon is nearly 50 times more abundant than doubly ionized argon. However, the ionization energies of Ar and Ar^+ are 15.76 and 27.6 eV, respectively, and hence not very different. The high line ratio can only be reconciled for high electron densities (lowering the recombination rate of Ar^{++}) and a very soft EUV field with $T \sim 20,000$ K. While model-calculated line ratios favor EUV production versus X-ray production (see Figure 4) of Ar ions, detailed models are needed for a more definitive conclusion.

The centimeter emission in excess of the dust thermal emission from the disk of T Cha provides an upper limit on the EUV luminosity impinging on the disk. This upper limit for T Cha is not stringent enough to exclude ionization of neon from soft EUV photons (Pascucci et al. 2014). This leads us to ask whether soft EUV can ionize both argon and neon in the disk of T Cha. Since EUV heated gas is at $\sim 10,000$ K, the gas temperature should be high even in the outer disk. As $[\text{Ne II}]$ and $[\text{Ar II}]$ have similar ionization potentials, they should have had similar spatial extent, which is counter to what we find for T Cha; i.e., $[\text{Ne II}]$ and $[\text{Ne III}]$ are spatially more extended than $[\text{Ar II}]$ (Section 3.2). Furthermore, it seems unlikely for soft EUV photons to be able to penetrate (go unabsorbed) through the compact wind component being traced by argon and ionize neon further out in the disk. It is particularly difficult for soft EUV to produce $[\text{Ne III}]$, which has a high ionization potential (~ 41 eV) and is found to be spatially more extended than argon in T Cha. Therefore, we conclude that the most likely scenario is that soft EUV ionizes argon, while neon is ionized by X-rays (either hard or soft spectrum); see sketch in Figure 5. This is in line with the higher penetration depths of X-rays with respect to EUV (Hollenbach & Gorti 2009) and the scenario put forward in Pascucci et al. (2020) for more evolved disks where any inner wind becomes more tenuous. Here, we assumed that like $[\text{Ne II}]$, $[\text{Ar II}]$ is also tracing a disk wind component, as the $[\text{Ar II}]$ 6.98 μm line is inaccessible with a high-resolution spectrograph to search for the signature line blueshift of a wind.

Sellek et al. (submitted) modeled winds in T Cha with EUV and X-ray spectra and attempted to constrain the spectrum using the line ratios and line luminosities obtained from this work. They find that adding a soft EUV component to the X-ray spectrum leads to a better match with the observed ratios of neon and argon, which is in agreement with the results from this work.

4.3. The Spatial Extent of Disk Winds Traced by Neon and Argon

As mentioned earlier, it is crucial to determine the origin of $[\text{Ne II}]$ emission (MHD versus PE wind) and, consequently, the wind mass-loss rate to constrain the time left for planet

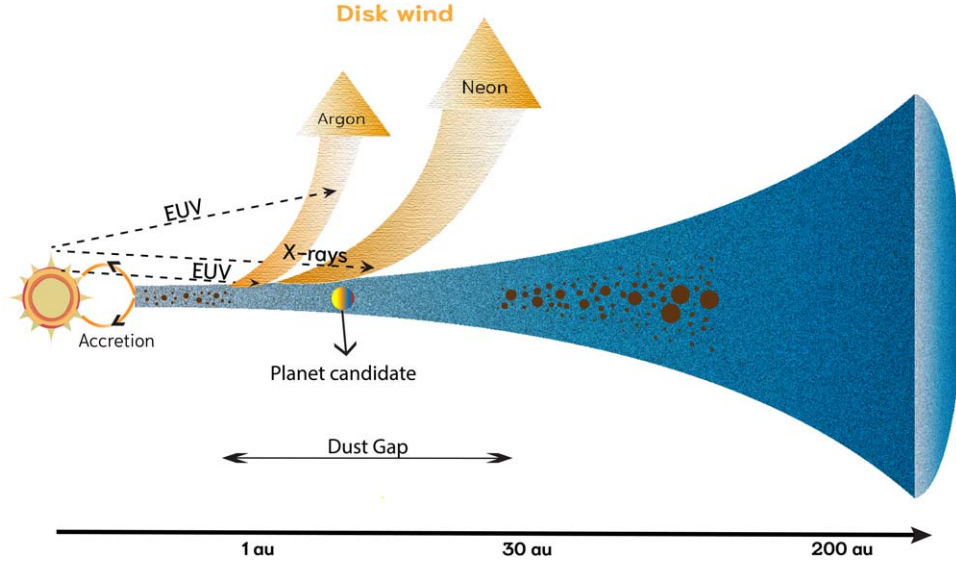


Figure 5. Sketch for T Cha highlighting the argon and neon ionization mechanisms as well as the relative spatial extent of the disk wind emission traced by the two species. EUV ionizes argon, but it is blocked by the wind component traced by argon. However, X-rays can penetrate this component and ionize neon further out in the disk; see the more evolved disk/wind systems in Pascucci et al. (2020). The location of the planet candidate is from Huélamo et al. (2011), and the dust gap is from Hendlar et al. (2018).

formation and migration. The spatial information on [Ne II] emission obtained in this work (Section 3.2) can provide us with useful constraints on its origin as well as the wind mass-loss rate estimates. To reiterate, T Cha has a large dust gap (Hendlar et al. 2018), and its [Ne II] emission shows a blueshift (Pascucci & Sterzik 2009; Sacco et al. 2012). This means that our view of the redshifted emission is blocked by either the very small inner dust disk (<1 au) or the outer disk (~ 25 au; e.g., Ercolano & Owen 2010; Pascucci et al. 2011). If the [Ne II] emission was spatially compact, then it would have eliminated its possibility of tracing a PE wind, but as we have seen in Sections 3.2.1 and 3.2.2, the [Ne II] emission is extended beyond the PSF and hence resolved. Moreover, we also see that [Ne III] is similarly extended beyond the PSF from Section 3.2.1. The difference in the extension direction between the continuum emission at $12.81 \mu\text{m}$ and [Ne II] emission provides spatial confirmation for [Ne II] tracing a disk wind. More importantly, this extension is compatible with the PE wind scenario as well as the MHD wind scenario. We also find, using both continuum and PSF subtraction, that [Ar II] traces a more compact emission. Having the spatial information of not just one but two possible wind-tracing emission lines can put a better constraint on the wind mass-loss rate and the wind launch radii, which in turn can provide insight into whether the wind is thermally driven or MHD-driven.

A simple estimate of the wind mass-loss rate (\dot{M}_W) can be obtained by assuming an EUV-driven fully ionized wind. It can be written as an integral of mass density \times wind velocity \times cross-section area. To get the mass density, we need the electron density, which can be obtained from Equation (4) of Font et al. (2004),

$$n_o = n_g \times \left(\frac{r}{r_g} \right)^{-3/2}, \quad (2)$$

where r_g is the gravitational radius and n_g is the base electron density at r_g and can be calculated using Equations (12) and

(13) of Font et al. (2004), respectively,

$$r_g \approx 1.3 \times 10^{14} \left(\frac{M_*}{1 M_\odot} \right) \text{cm}, \quad (3)$$

$$n_g \approx 4 \times 10^4 \left(\frac{M_*}{1 M_\odot} \right)^{-3/2} \left(\frac{\Phi_{\text{EUV}}}{10^{41} \text{s}^{-1}} \right)^{1/2} \text{cm}^{-3}, \quad (4)$$

where M_* is the stellar mass and Φ_{EUV} is the stellar EUV flux. For T Cha, we use a stellar mass of $1.5 M_\odot$ (Olofsson et al. 2011), and we have the EUV flux upper limit from Pascucci et al. (2014) calculated using centimeter free-free emission as $4.1 \times 10^{41} \text{s}^{-1}$. Substituting these values in Equations (3) and (4) gives $r_g \sim 13$ au and the electron density there of $\sim 4 \times 10^4 \text{cm}^{-3}$, respectively. Substituting these values in Equation (2) provides the base electron density only as a function of radius. Using this, we can write the total mass-loss rate as

$$\dot{M}_W = \int_{0.1r_g}^{r_{\text{max}}} \mu m_{\text{H}} n_o \times v_w \times 4\pi r dr, \quad (5)$$

where μ is the mean molecular weight (1.35), m_{H} is the mass of a hydrogen atom, n_o is substituted from Equation (2), v_w is the speed of the wind leaving the disk, $0.1r_g$ is the wind launch radii (e.g., Alexander 2008), and r_{max} is the maximum radial extent of the observed [Ne II] emission. The blueshift observed in the high spectral resolution [Ne II] spectrum, after accounting for inclination, can be taken as the wind speed—for T Cha, this is $\sim 12 \text{km s}^{-1}$ (4km s^{-1} blueshift and 70° inclination; Pascucci & Sterzik 2009; Huélamo et al. 2015, respectively). We can take r_{max} as the quadrature subtraction of the [Ne II] half-width at half-maximum (HWHM) and the PSF HWHM in the vertical (\sim disk) direction of ~ 6.5 au (see Section 3.2.2). Integrating Equation (5) and substituting the above values provides a wind mass-loss rate of $\sim 6.5 \times 10^{-10} M_\odot \text{yr}^{-1}$. Note that this estimate has an uncertainty of at least a factor of 2, propagated by the uncertainty in the stellar EUV flux (Pascucci et al. 2014). If the wind is indeed EUV-driven, the above

estimate will act as an upper limit since we only have the upper limit for EUV flux. At the same time, if the wind is not fully ionized, the mass-loss rate will be higher than the above estimate. Detailed modeling is carried out by Sellek et al. (submitted) using the line luminosities, line ratios, and spatial extent of the lines detected in this work to estimate the wind mass-loss rate as well as the wind launch radii.

4.4. Location and Nature of the Spatially Extended PAH Features

PAHs are constituted of multiple interconnected benzene rings and are known to play a major role in the chemistry of the disk atmosphere (e.g., Anderson et al. 2017) as they influence the ionization state of the gas (Thi et al. 2019). Their ability to efficiently convert incident far-UV radiation into thermal energy due to a high photoelectric yield (Bakes & Tielens 1994) significantly impacts atmospheric mass-loss rates (e.g., Gorti et al. 2009). Since PAHs have high opacity at UV wavelengths, their radial distribution provides important information on the UV radiation field in the inner and outer disk (e.g., Geers et al. 2007).

We found that the PAH features in T Cha are more extended than the nearby continuum (Section 3.2). They are found to be extended in the disk direction (vertical cut) instead of the wind direction (horizontal cut), suggesting that they are not being carried away in the wind but could still be transported by the stellar radiation along the disk surface. We also cannot exclude the possibility of the PAHs originating at the base of the wind. Geers et al. (2007) detected the 3.3 and 11.2 μm PAH features using the ISAAC *L*-band and VISIR *N*-band spectra of T Cha. Since both emissions were spatially unresolved, they provided an upper limit on the radial extent of these PAH emissions of 35 and 20 au, respectively. Olofsson et al. (2013) modeled the dust disk of T Cha including the PAH emission and compared the model results to observations carried out with VLTI/MIDI and NACO/SAM. They suggested that PAH molecules cannot be located at the inner edge of the outer disk (~ 12 au), as they would be too efficient at backward scattering (which is not observed) and might have been transported outward by radiation pressure or stellar wind. Although they could not provide an estimate of how radially extended the PAHs are, the fact that we found PAH emission more extended (~ 37 au along the disk) than the continuum is consistent with their argument.

Particularly for transition disks, Maaskant et al. (2014) found strong correlations between the relative integrated fluxes of the 6.2 and 11.2 μm PAH features and their spatial extent. To infer this extent, they used VLT/VISIR and compared the FWHM of the spatially resolved PAH emission with the *N*-band continuum. They found that in the case of stronger 6.2 μm than 11.2 μm flux ($I_{6.2}/I_{11.2} \sim 2-4$), the PAH emission is dominated by the inner regions including the dust gap. For similar strengths of the two features ($I_{6.2}/I_{11.2} \sim 1-2$), most PAH emission arises in the outer disk with some possible emission in the dust cavity. And finally, for a stronger 11.2 μm feature than 6.2 μm ($I_{6.2}/I_{11.2} < 1$), the PAHs are more extended outward and dominate only in the outer disk. Maaskant et al. (2014) modeled the PAH emission from four of these disks and found that having ionized PAHs in the dust gap increases the $I_{6.2}/I_{11.2}$ ratio and that a value of ~ 1 can be explained by neutral PAHs. For T Cha, we find $I_{6.2}/I_{11.2} \sim 0.9$ (see Table 1), suggesting similar strengths for the two features. Therefore, PAHs being

spatially extended in the MIRI MRS cubes is consistent with the trend observed by Maaskant et al. (2014). The ratio also means that the PAHs in the disk of T Cha are predominantly neutral.

Geers et al. (2006) analyzed the Spitzer-IRS-detected 11.2 μm PAH feature toward T Cha. They noticed that this feature is both broader and redshifted compared to a typical ISM PAH feature, which peaks in the wavelength range of 11.2–11.24 μm and has a width of ~ 0.17 μm . With the better resolution of MIRI MRS compared to Spitzer IRS, we find that the 11.2 μm feature in the JWST spectra peaks at ~ 11.29 μm , and a Gaussian fit gives a width of ~ 0.25 μm . Due to the lack of crystalline silicate features, the possibility of the 11.2 μm crystalline silicate feature contributing to the broadening was eliminated, and it was rather shown that a model including a combination of fundamental and hot bands of PAH transition could explain the feature (Geers et al. 2006). Recently, Mackie et al. (2022) showed that the anharmonic interactions between different rotational modes of PAHs shift the emission spectra to higher wavelengths and broaden by the factor seen in several observations (e.g., Orion Bar; Peeters et al. 2002; van Dienenhoven et al. 2004). This reasoning was also strongly supported by the recent MIRI MRS observations of PAHs in the Orion Bar (Chown et al. 2023).

5. Summary and Conclusions

Using JWST MIRI MRS, we observed T Cha, a G8 spectral type star surrounded by a disk with a dust gap (~ 20 au). It is known to have a small blueshift ($\sim 3-6$ km s $^{-1}$) in its [Ne II] line at 12.8 μm indicating a slow wind that is at least partly ionized. We retrieved the IFU cube for T Cha over the complete MRS wavelength range of $\sim 5-28$ μm . We extracted the spectrum over $2.5 \times$ PSF and searched for gas emission lines. We also performed spaxel-by-spaxel continuum subtraction in the image plane of T Cha to test if the strongest emission lines are spatially extended. On the continuum-subtracted line image, we performed a 2D Gaussian fit to determine the emission size and compare it with the extension of the standard star/PSF. Finally, we performed PSF subtraction on these continuum-subtracted images and retrieved the PSF-subtracted maps of [Ne II] and [Ar II]. The main conclusions from this work are listed below.

1. In addition to [Ne II], which was previously detected and known to trace a wind, we report for the first time detections of [Ar II] at 6.98 μm , [Ar III] at 8.99 μm , and [Ne III] at 15.55 μm . We also find individual PAH features (6.02 and 8.22 μm) as well as PAH complexes (6.2, 7.7, 8.6, 11.3, 12, and 12.7 μm), of which only the 11.3 μm complex was previously detected for T Cha. Additionally, we also detect the H $_2$ v0-0 S(3) line in the spectrum of T Cha.
2. We find that the MIRI [Ne II] flux is 50% higher than the Spitzer flux obtained in 2006. The amplitude of [Ne II] variability (50%) is smaller than that observed for [O I] ($\sim 230\%$), and it is unclear whether variabilities in these two lines are correlated to each other or not. Future simultaneous observations of both lines can help us understand the evolution of these wind diagnostic lines better.
3. By using the [Ne II]/[Ne III] and [Ar II]/[Ar III] line ratios and ionization model predictions from Hollenbach &

Gorti (2009), it is most likely that argon is being ionized by EUV, while neon is being ionized by X-rays in T Cha. However, soft X-ray ionization of argon cannot be ruled out just yet.

4. We find that [Ne II] and [Ne III] trace extended emission beyond the PSF, while [Ar II] traces a relatively compact emission in T Cha.
5. We also find that the PAH emission is spatially more extended than the continuum, suggesting that the emission is dominated in the outer disk surface. Based on the relative strengths of the 6.2 and 11.2 μm features, we find that the PAH emission is mostly neutral.

T Cha is the first protoplanetary disk for which four forbidden noble gas lines are detected together, as well as the first detection of [Ar III]. We suggest that the higher MIRI [Ne II] flux could result from an increased wind mass-loss rate, more heating, or higher fractional ionization caused by higher radiation received by the outer disk. The more compact emission traced by [Ar II] can act as a screen for photons ionizing Ne and Ne^+ atoms further out in the disk; see Figure 5. This is in agreement with argon being ionized by EUV and Ne and Ne^+ being ionized by X-rays. At the same time, the spatial extension of the [Ne II] and [Ne III] emission is consistent with both a PE wind and an MHD wind. However, T Cha is a weak accretor that shows no evidence of a jet and has a relatively weak but broad ($\text{FWHM} \sim 47 \text{ km s}^{-1}$) [O I] 6300 \AA line centered at the stellar velocity and a mid-infrared spectrum dominated by ionic lines. Putting this information together suggests that T Cha might represent the more evolved wind/disk stage shown in the bottom panel of Figure 9 of Pascucci et al. (2020). The [O I] would be tracing a very close-in but tenuous MHD wind, while ionized argon and neon may be tracing a PE wind further out, with argon tracing a more compact wind structure than neon. This picture is in agreement with results from the radiative transfer photoionization models of disk winds in T Cha presented in A. Sellek et al. (2024, in preparation). Detailed modeling combining MHD and PE winds is necessary to further test this evolutionary scenario put forward for T Cha. Additional MIRI MRS observations of low accreting stars with gapped disks will be critical to determine the prevalence of spatially extended winds traced by ions, as observed in T Cha.

Acknowledgments

This work is based on observations made with the NASA/ESA/CSA James Webb Space Telescope. The data were obtained from the Mikulski Archive for Space Telescopes at the Space Telescope Science Institute, which is operated by the Association of Universities for Research in Astronomy, Inc., under NASA contract NAS 5-03127 for JWST. The observations are associated with JWST GO Cycle 1 program ID 2260. The JWST data used in this paper can be found in MAST:10.17909/dhmf-fx64. This work was funded by NASA/STScI GO grant JWST-GO-02260.001. A.D.S. was supported by the European Union's Horizon 2020 research and innovation

program under Marie Skłodowska-Curie grant agreement No. 823823 (DUSTBUSTERS). G.B. has received funding from the European Research Council (ERC) under the European Union's Horizon 2020 Framework Programme (grant agreement No. 853022, PEVAP). N.S.B. thanks Arin Avsar for the useful discussion on the PSF subtraction technique. N.S.B. acknowledges the quick response and support from the JWST MIRI support team at STScI. R.A. acknowledges funding from the Science & Technology Facilities Council (STFC) through consolidated grant ST/W000857/1. A.D.S. acknowledges the support of a Science and Technology Facilities Council (STFC) PhD studentship and funding from the European Research Council (ERC) under the European Union's Horizon 2020 research and innovation program (grant agreement No. 1010197S1 MOLDISK). This work is based in part on archival observations made with the Spitzer Space Telescope, which was operated by the Jet Propulsion Laboratory, California Institute of Technology, under a contract with NASA. This work has also made use of data from the European Space Agency (ESA) mission Gaia <https://www.cosmos.esa.int/gaia>, processed by the Gaia Data Processing and Analysis Consortium (DPAC; <https://www.cosmos.esa.int/web/gaia/dpac/consortium>). Funding for the DPAC has been provided by national institutions, in particular, the institutions participating in the Gaia Multilateral Agreement.

Facilities: JWST, Spitzer, Gaia

Software: Astropy (Astropy Collaboration et al. 2013, 2018, 2022), CASA (McMullin et al. 2007), JWST (Bushouse et al. 2023), Matplotlib (Hunter 2007), NumPy (van der Walt et al. 2011), Photutils (Bradley et al. 2022), SciPy (Virtanen et al. 2020).

Appendix A Gaussian Fit to Lines

We fit Gaussian profiles to the lines listed in Table 1 and plot them in Figure 6. [Ar III] has a 4σ detection, whereas other lines, except H I (7-6), have $\geq 10\sigma$ detections. Since each subplot has an equal x -axis length, the width of the Gaussian profile increases with wavelength as the spectral resolution degrades with increasing wavelength. This can be seen in Figure 6, where the width is smallest for [Ar II] 6.98 μm and largest for [Ne III] 15.55 μm , as expected. For H I (7-6), while there is an emission with a peak amplitude of $\sim 3\sigma$ at its position, the width of the fitted line is ~ 3 times the spectral resolution of MIRI MRS ($\sim 100 \text{ km s}^{-1}$) at that wavelength, which is rather unrealistic. Hence, we report H I (7-6) as a nondetection and provide an upper limit. To cross-check the [Ar III] detection, we compare spectra from different reductions by switching the `residual_fringe` step on and off. We also extract spectra using different apertures ($1.5 \times \text{FWHM}$ – $3 \times \text{FWHM}$, in four steps) and calculate the [Ar III] line flux in each, finding that the line is always present and its flux varies within the uncertainties.

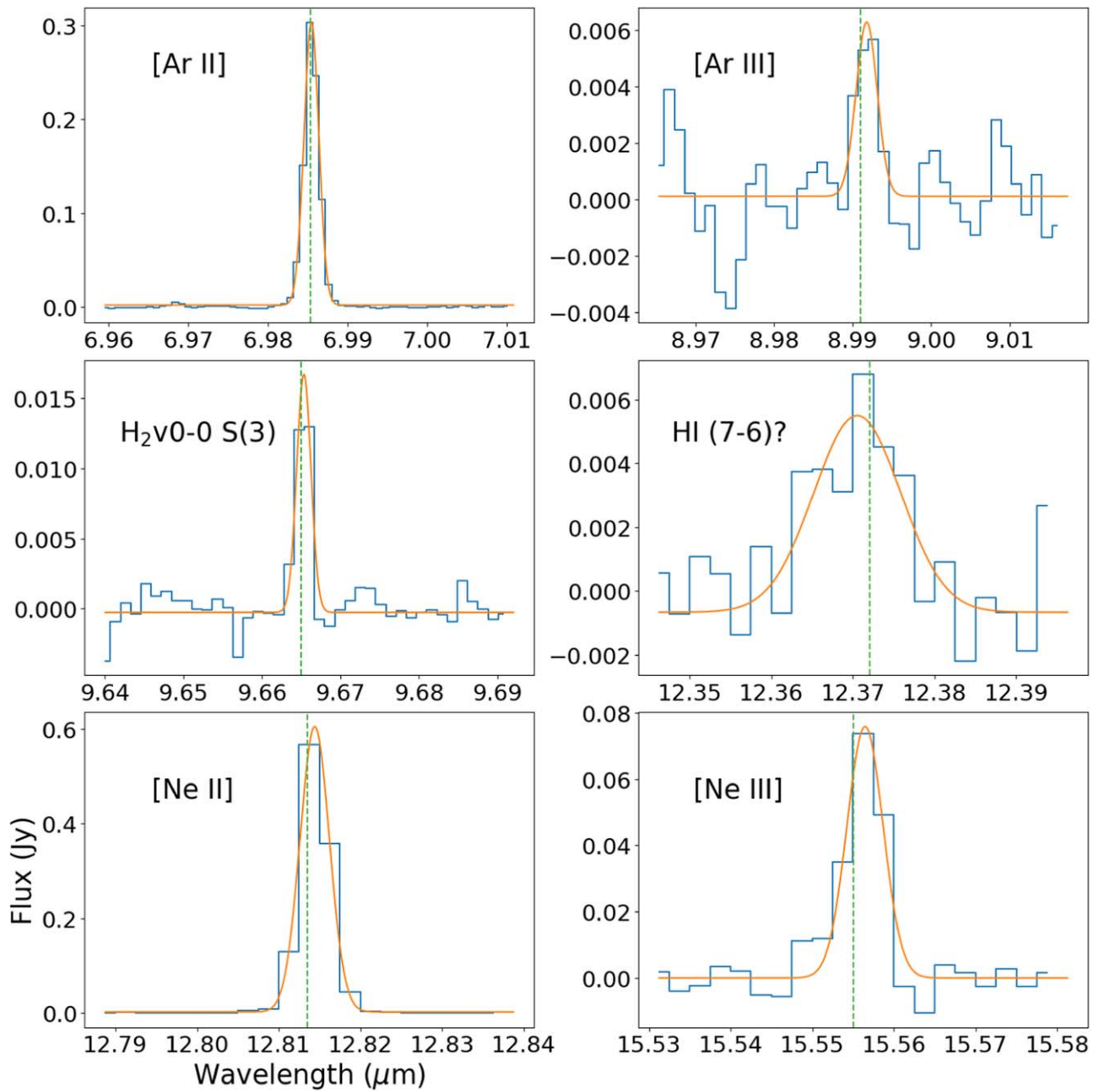


Figure 6. The figure shows JWST MIRI MRS spectral profiles for the lines listed in Table 1 in blue and the performed Gaussian fit in orange. The green dashed line indicates the rest wavelength of the transition. Each subplot has the same length of the wavelength range ($\sim 0.055 \mu\text{m}$) plotted on the x -axis with the lines peaking at the center.

Appendix B PSF Subtraction Using HD 167060

This section shows the PSF subtraction results obtained by following the same method followed in Section 3.2.2 but using the standard star HD 167060 as the PSF instead of HD 37962. The results are plotted in Figure 7. At $12.81 \mu\text{m}$, both the continuum and [Ne II] show emission beyond the PSF and have different directions of extension, consistent with the results

described in the main text. Similarly, at $7 \mu\text{m}$, the continuum is very slightly resolved, and [Ar II] shows very compact unresolved emission. A slight difference in the emission structure at $7 \mu\text{m}$ arises due to the PSF's left shoulder showing extra emission. This could be due to either a centroid fitting error or an interpolation error during image shifting. In either case, our results remain unaffected, and we are able to strongly demonstrate the independence of our results to the small PSF variations.

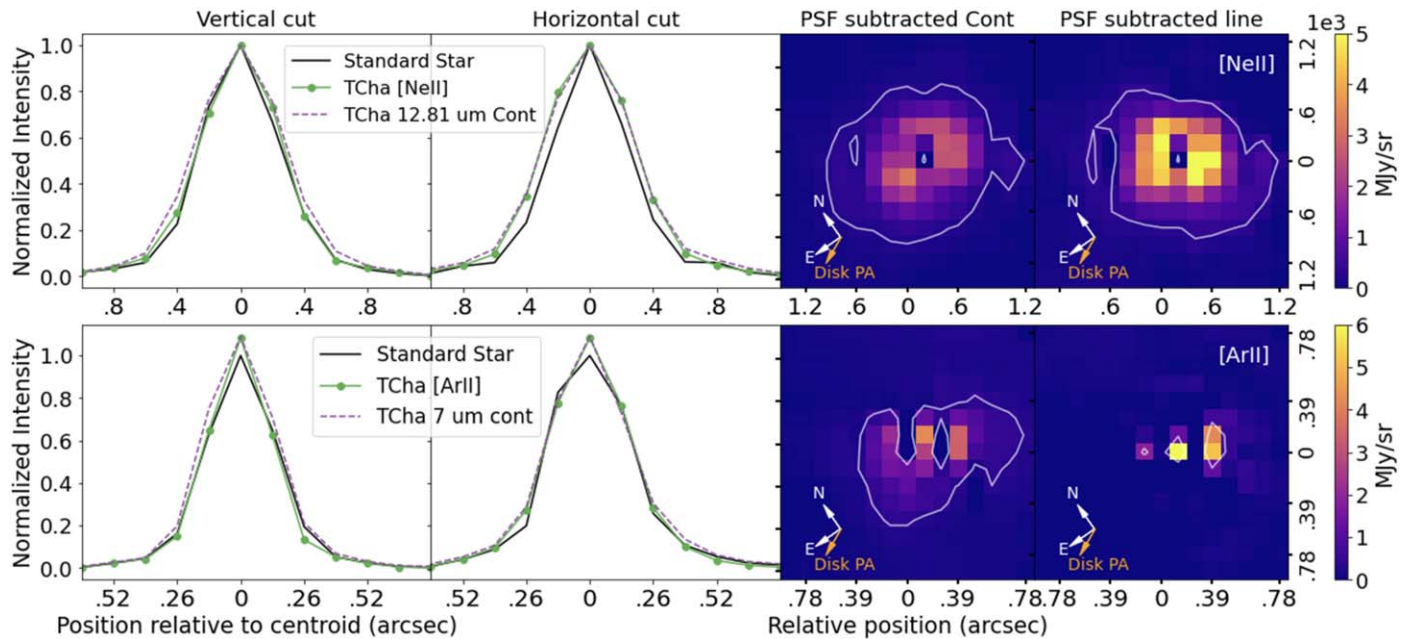


Figure 7. The left two panels compare the radial profiles of continuum and continuum-subtracted lines with the PSF (standard star HD 167060) in the horizontal and vertical directions. The two panels on the right show the PSF-subtracted images of the continuum at 12.81 and $7 \mu\text{m}$ and the [Ne II] and [Ar II] lines. The white contours in the images follow 5σ emission.

Appendix C Extended PAH Emission

This section presents a PSF comparison with the continuum-subtracted PAH emission feature at $6.2\ \mu\text{m}$ by following the procedure detailed in Section 3.2.2. Here, we use the standard star HD 37962 as the PSF, as is done for all the results in the main text. We show the vertical and horizontal profiles of the PSF, continuum, and continuum-subtracted PAH in Figure 8. It

can be easily seen that the PAH emission is extended beyond the PSF and the continuum in the vertical cut/profile. In terms of the direction of extension, this is consistent with the results shown in Section 3.2.2 and Appendix B, where the continuum, when extended, is extended in the vertical profiles and wind in the horizontal profile. Since PAH is supposed to be tracing the disk surface, it should be extended mainly in the vertical profile, which is what we see in Figure 8.

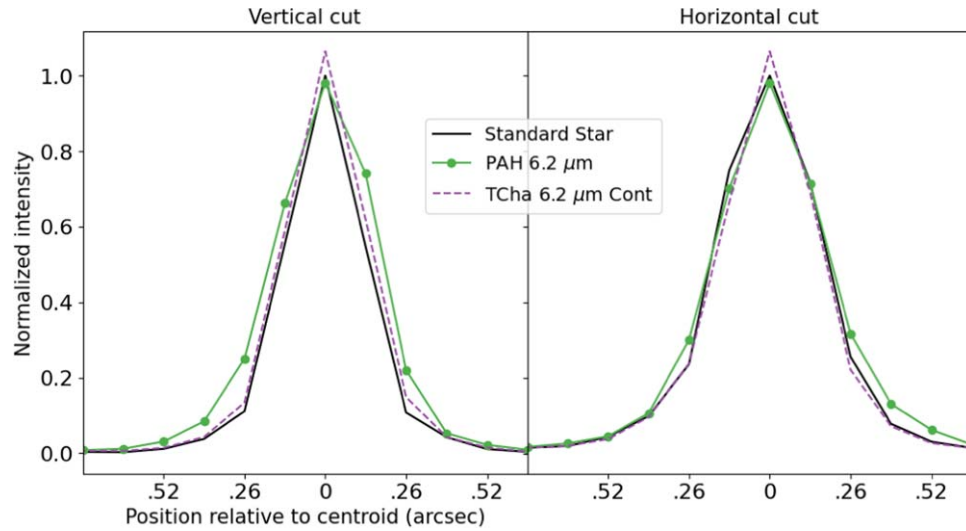


Figure 8. The two panels compare the radial profiles of continuum and continuum-subtracted PAH emission with the PSF/standard star in the horizontal and vertical directions.

ORCID iDs

Naman S. Bajaj  <https://orcid.org/0000-0003-3401-1704>
 Ilaria Pascucci  <https://orcid.org/0000-0001-7962-1683>
 Richard Alexander  <https://orcid.org/0000-0001-6410-2899>
 Andrew Sellek  <https://orcid.org/0000-0003-0330-1506>
 Andras Gaspar  <https://orcid.org/0000-0001-8612-3236>
 Cathie Clarke  <https://orcid.org/0000-0003-4288-0248>
 Chengyan Xie  <https://orcid.org/0000-0001-8184-5547>
 Giulia Ballabio  <https://orcid.org/0000-0002-4687-2133>
 Dingshan Deng  <https://orcid.org/0000-0003-0777-7392>

References

- Alcala, J. M., Covino, E., Franchini, M., et al. 1993, *A&A*, **272**, 225
 Alexander, R., Pascucci, I., Andrews, S., Armitage, P., & Cieza, L. 2014, in *Protostars and Planets VI*, ed. H. Beuther et al. (Tucson, AZ: Univ. Arizona Press), 475
 Alexander, R. D. 2008, *MNRAS*, **391**, L64
 Anderson, D. E., Bergin, E. A., Blake, G. A., et al. 2017, *ApJ*, **845**, 13
 Argyriou, I., Glasse, A., Law, D. R., et al. 2023, *A&A*, **675**, A111
 Astropy Collaboration, Price-Whelan, A. M., Lim, P. L., et al. 2022, *ApJ*, **935**, 167
 Astropy Collaboration, Price-Whelan, A. M., Sipőcz, B. M., et al. 2018, *AJ*, **156**, 123
 Astropy Collaboration, Robitaille, T. P., Tollerud, E. J., et al. 2013, *A&A*, **558**, A33
 Bae, J., Isella, A., Zhu, Z., et al. 2023, in *ASP Conf. Ser. 534, Protostars and Planets VII*, ed. S. Inutsuka et al. (San Francisco, CA: ASP), 423
 Bakes, E. L. O., & Tielens, A. G. G. M. 1994, *ApJ*, **427**, 822
 Baldovin-Saavedra, C., Audard, M., Carmona, A., et al. 2012, *A&A*, **543**, A30
 Banzatti, A., Meyer, M. R., Bruderer, S., et al. 2012, *ApJ*, **745**, 90
 Banzatti, A., Pascucci, I., & Edwards, S. 2018, *AAS Meeting Abstracts*, 231, 229.01
 Banzatti, A., Pascucci, I., Edwards, S., et al. 2019, *ApJ*, **870**, 76
 Beck, T. L., & Bary, J. S. 2019, *ApJ*, **884**, 159
 Béthune, W., Lesur, G., & Ferreira, J. 2017, *A&A*, **600**, A75
 Bradley, L., Sipőcz, B., Robitaille, T., et al. 2022, *astropy/photutils*: v1.6.0, Zenodo, doi:10.5281/zenodo.7419741
 Bushouse, H., Eisenhamer, J., Dencheva, N., et al. 2023, *JWST Calibration Pipeline*, v1.11.2, Zenodo, doi:10.5281/zenodo.8140011
 Cahill, E., Whelan, E. T., Huéllamo, N., & Alcalá, J. 2019, *MNRAS*, **484**, 4315
 Chavarria, C., Covino, E., Franchini, M., Stalio, R., & Terranegra, L. 1989, *Msngr*, **58**, 35
 Chown, R., Sidhu, A., Peeters, E., et al. 2023, arXiv:2308.16733
 Clarke, C. J., & Alexander, R. D. 2016, *MNRAS*, **460**, 3044
 Clarke, C. J., Gendrin, A., & Sotomayor, M. 2001, *MNRAS*, **328**, 485
 Covino, E., Terranegra, L., Franchini, M., Chavarria, K. C., & Franchini, R. 1992, *A&AS*, **94**, 273
 Covino, E., Terranegra, L., Magazzu, A., et al. 1996, in *ASP Conf. Ser. 109, Cool Stars, Stellar Systems, and the Sun*, ed. R. Pallavicini & A. K. Dupree (San Francisco, CA: ASP), 421
 Dickson-Vandervelde, D. A., Wilson, E. C., & Kastner, J. H. 2021, *AJ*, **161**, 87
 Ercolano, B., & Owen, J. E. 2010, *MNRAS*, **406**, 1553
 Ercolano, B., & Pascucci, I. 2017, *RSOS*, **4**, 170114
 Espaillat, C., Calvet, N., D'Alessio, P., et al. 2007, *ApJL*, **664**, L111
 Espaillat, C., Furlan, E., D'Alessio, P., et al. 2011, *ApJ*, **728**, 49
 Espaillat, C., Ingleby, L., Furlan, E., et al. 2013, *ApJ*, **762**, 62
 Espaillat, C. C., Thanathibodee, T., Pittman, C. V., et al. 2023, *ApJL*, **958**, L4
 Fang, M., Pascucci, I., Edwards, S., et al. 2023a, *ApJ*, **945**, 112
 Fang, M., Wang, L., Herczeg, G. J., et al. 2023b, *NatAs*, **7**, 905
 Fernández, D., Figueras, F., & Torra, J. 2008, *A&A*, **480**, 735
 Font, A. S., McCarthy, I. G., Johnstone, D., & Ballantyne, D. R. 2004, *ApJ*, **607**, 890
 Gaia Collaboration, Vallenari, A., Brown, A. G. A., et al. 2023, *A&A*, **674**, A1
 Geers, V. C., Augereau, J. C., Pontoppidan, K. M., et al. 2006, *A&A*, **459**, 545
 Geers, V. C., van Dishoeck, E. F., Visser, R., et al. 2007, *A&A*, **476**, 279
 Glassgold, A. E., Najita, J. R., & Igea, J. 2007, *ApJ*, **656**, 515
 Gordon, K. D., Bohlin, R., Sloan, G. C., et al. 2022, *AJ*, **163**, 267
 Gorti, U., Dullemond, C. P., & Hollenbach, D. 2009, *ApJ*, **705**, 1237
 Gorti, U., Liseau, R., Sándor, Z., & Clarke, C. 2016, *SSRv*, **205**, 125
 Gressel, O., Turner, N. J., Nelson, R. P., & McNally, C. P. 2015, *ApJ*, **801**, 84
 Hartmann, L., Herczeg, G., & Calvet, N. 2016, *ARA&A*, **54**, 135
 Hendler, N. P., Pinilla, P., Pascucci, I., et al. 2018, *MNRAS*, **475**, L62
 Herczeg, G. J., Najita, J. R., Hillenbrand, L. A., & Pascucci, I. 2007, *ApJ*, **670**, 509
 Hollenbach, D., & Gorti, U. 2009, *ApJ*, **703**, 1203
 Hollenbach, D., Johnstone, D., Lizano, S., & Shu, F. 1994, *ApJ*, **428**, 654
 Huéllamo, N., de Gregorio-Monsalvo, I., Macias, E., et al. 2015, *A&A*, **575**, L5
 Huéllamo, N., Lacour, S., Tuthill, P., et al. 2011, *A&A*, **528**, L7
 Hunter, J. D. 2007, *CSE*, **9**, 90
 Kessler-Silacci, J., Augereau, J.-C., Dullemond, C. P., et al. 2006, *ApJ*, **639**, 275
 Lahuis, F., van Dishoeck, E. F., Blake, G. A., et al. 2007, *ApJ*, **665**, 492
 Law, D. D., Morrison, J. E., Argyriou, I., et al. 2023, *AJ*, **166**, 45
 Lesur, G. 2021, *JPIPh*, **87**, 20587010
 Lesur, G., Flock, M., Ercolano, B., et al. 2023, in *ASP Conf. Ser. 534, Astronomical Society of the Pacific Conference Series*, ed. S. Inutsuka et al. (San Francisco, CA: ASP), 465
 Maaskant, K. M., Min, M., Waters, L. B. F. M., & Tielens, A. G. G. M. 2014, *A&A*, **563**, A78
 Mackie, C. J., Candian, A., Lee, T. J., & Tielens, A. G. G. M. 2022, *JPCA*, **126**, 3198
 McGinnis, P., Dougados, C., Alencar, S. H. P., Bouvier, J., & Cabrit, S. 2018, *A&A*, **620**, A87
 McMullin, J. P., Waters, B., Schiebel, D., Young, W., & Golap, K. 2007, in *ASP Conf. Ser. 376, Astronomical Data Analysis Software and Systems XVI*, ed. R. A. Shaw, F. Hill, & D. J. Bell (San Francisco, CA: ASP), 127
 Murphy, S. J., Lawson, W. A., & Bessell, M. S. 2013, *MNRAS*, **435**, 1325
 Nisini, B., Antonucci, S., Alcalá, J. M., et al. 2018, *A&A*, **609**, A87
 Olofsson, J., Benisty, M., Augereau, J. C., et al. 2011, *A&A*, **528**, L6
 Olofsson, J., Benisty, M., Le Bouquin, J. B., et al. 2013, *A&A*, **552**, A4
 Ortega, V. G., Jilinski, E., de la Reza, R., & Bazzanella, B. 2009, *AJ*, **137**, 3922
 Pascucci, I., Apai, D., Hardegree-Ullman, E. E., et al. 2008, *ApJ*, **673**, 477
 Pascucci, I., Banzatti, A., Gorti, U., et al. 2020, *ApJ*, **903**, 78
 Pascucci, I., Cabrit, S., Edwards, S., et al. 2023, in *ASP Conf. Ser. 534, Protostars and Planets VII*, ed. S. Inutsuka et al. (San Francisco, CA: ASP), 567
 Pascucci, I., Hollenbach, D., Najita, J., et al. 2007, *ApJ*, **663**, 383
 Pascucci, I., Ricci, L., Gorti, U., et al. 2014, *ApJ*, **795**, 1
 Pascucci, I., & Sterzik, M. 2009, *ApJ*, **702**, 724
 Pascucci, I., Sterzik, M., Alexander, R. D., et al. 2011, *ApJ*, **736**, 13
 Peeters, E., Hony, S., Van Kerckhoven, C., et al. 2002, *A&A*, **390**, 1089
 Pohl, A., Sissa, E., Langlois, M., et al. 2017, *A&A*, **605**, A34
 Pringle, J. E. 1981, *ARA&A*, **19**, 137
 Rab, C., Weber, M., Picogna, G., et al. 2023, *ApJL*, **955**, L11
 Rigliaco, E., Pascucci, I., Duchene, G., et al. 2015, *ApJ*, **801**, 31
 Ruaud, M., & Gorti, U. 2019, *ApJ*, **885**, 146
 Ruden, S. P., & Pollack, J. B. 1991, *ApJ*, **375**, 740
 Sacco, G. G., Flaccomio, E., Pascucci, I., et al. 2012, *ApJ*, **747**, 142
 Schisano, E., Covino, E., Alcalá, J. M., et al. 2009, *A&A*, **501**, 1013
 Simon, M. N., Pascucci, I., Edwards, S., et al. 2016, *ApJ*, **831**, 169
 Szulágyi, J., Pascucci, I., Ábrahám, P., et al. 2012, *ApJ*, **759**, 47
 Testi, L., Birmstiel, T., Ricci, L., et al. 2014, in *Protostars and Planets VI*, ed. H. Beuther et al. (Tucson, AZ: Univ. Arizona Press), 339
 Thi, W. F., Lesur, G., Woitke, P., et al. 2019, *A&A*, **632**, A44
 van der Walt, S., Colbert, S. C., & Varoquaux, G. 2011, *CSE*, **13**, 22
 van Dienenhoven, B., Peeters, E., Van Kerckhoven, C., et al. 2004, *ApJ*, **611**, 928
 Virtanen, P., Gommers, R., Burovski, E., et al. 2020, *scipy/scipy: SciPy v1.5.3*, Zenodo, doi:10.5281/zenodo.4100507
 Walter, F. M., Brown, A., France, K., et al. 2018, 20th Cambridge Workshop on Cool Stars, Stellar Systems and the Sun, Cambridge Workshop on Cool Stars, Stellar Systems, and the Sun, 77, doi:10.5281/zenodo.1489081
 Wells, M., Pel, J. W., Glasse, A., et al. 2015, *PASP*, **127**, 646
 Wölfer, L., Facchini, S., van der Marel, N., et al. 2023, *A&A*, **670**, A154
 Wright, E. L., Eisenhardt, P. R. M., Mainzer, A. K., et al. 2010, *AJ*, **140**, 1868